

## Density and atomic number measurements with spectral x-ray attenuation method

B. J. Heismann, J. Leppert, and K. Stierstorfer

Citation: [Journal of Applied Physics](#) **94**, 2073 (2003); doi: 10.1063/1.1586963

View online: <http://dx.doi.org/10.1063/1.1586963>

View Table of Contents: <http://scitation.aip.org/content/aip/journal/jap/94/3?ver=pdfcov>

Published by the [AIP Publishing](#)

---



## Re-register for Table of Content Alerts

Create a profile.



Sign up today!



# Density and atomic number measurements with spectral x-ray attenuation method

B. J. Heismann,<sup>a)</sup> J. Leppert, and K. Stierstorfer

Computed Tomography, Siemens Medical Solutions, Siemensstrasse 1, 91301 Forchheim, Germany

(Received 14 August 2002; accepted 7 May 2003)

X-ray attenuation measurements are widely used in medical and industrial applications. The usual results are one- to three-dimensional representations of the attenuation coefficient  $\mu(\mathbf{r})$ . In this paper, we present the  $\rho Z$  projection algorithm for obtaining the density  $\rho(\mathbf{r})$  and atomic number  $Z(\mathbf{r})$  with an energy-resolving x-ray method. As input data the algorithm uses at least two measurements  $\mu_1, \mu_2, \dots$  with different spectral weightings of the source spectrum  $S(E)$  and/or detector sensitivity  $D(E)$ . Analytically,  $\rho$  is a function of  $\mu_1 - c\mu_2$ ,  $c = \text{const}$ , and  $Z$  is a function of  $\mu_1/\mu_2$ . The full numerical treatment yields  $\rho(\mu_1, \mu_2)$  and  $Z(\mu_1, \mu_2)$  with  $S(E)$  and  $D(E)$  as commutative parametric functions. We tested the method with dual-energy computed tomography measurements of an organic sample and a set of chemical solutions with predefined  $\rho$  and  $Z$ . The resulting images show  $\rho$  and  $Z$  as complementary information: The density  $\rho$  reflects the morphology of the objects, whereas the atomic number  $Z = \text{number of electrons/atom}$  describes the material distribution. For our experimental setup we obtain an absolute precision of 0.1 for  $Z$  and 20 mg/cm<sup>3</sup> for  $\rho$ . The  $\rho Z$  projection can potentially lead to these classes of quantitative information for various scientific, industrial, and medical applications. © 2003 American Institute of Physics. [DOI: 10.1063/1.1586963]

## I. INTRODUCTION

X-ray imaging techniques range from linear scanning systems for, e.g., food or baggage inspection, to three-dimensional (3D) computed tomography (CT) scanners used in medical health care. All these imaging systems basically measure the linear attenuation coefficient  $\mu(\mathbf{r})$  of the scanned object. Mostly, a direct representation of a  $\mu(\mathbf{r})$  image is used for inspection and diagnosis.

In our field of work of medical CT imaging,  $\mu$  is commonly normalized to the attenuation of water by

$$C = 1000 \frac{\mu - \mu_{\text{water}}}{\mu_{\text{water}}}. \quad (1)$$

Thus  $C(\text{air}) = -1000$  HU and  $C(\text{water}) = 0$  with HU = dimensionless Hounsfield units. Table I shows ranges of  $C$  for different components of the human body.

Medical CT diagnosis mostly relies on spatial contrast in the attenuation  $C(\mathbf{r})$ , i.e., on its *relative* local changes. The *absolute*  $C$  is used rarely. Calcium scoring of blood vessel plaques<sup>1</sup> and bone densitometry<sup>2</sup> are examples. The former incorporates a  $C$  thresholding for calculating the empirical Agatston score, whereas the latter uses calibrated tables transforming  $C$  into density values.

Alvarez and Macovski<sup>3</sup> initially investigated the energy dependence of  $\mu$  for CT: They showed that a separation into photoeffect absorption and Compton scattering contributions is feasible by spectral measurements. The so-called base material decomposition yields additional contrasts in two or

more virtual “pure” material images. Still, it provides only qualitative values.

In this paper we directly aim at the functional dependency of the attenuation process. For given spectral source  $S(E)$  and detector characteristics  $D(E)$  of the measurement, the mass density  $\rho$  and effective atomic number  $Z$  of the absorber completely determine the measured attenuation coefficient  $\mu$ , i.e.,  $\mu = \mu(\rho, Z)$ .

It is important to note that  $\rho$  and  $Z$  represent completely different properties: The density  $\rho = dm/dV$  describes the mass distribution, i.e., the morphology of the absorber. The effective  $Z$ , however, reflects the average number of electrons per atom. This is a characteristic value for any kind of material, including compounds. For pure materials it exactly matches the atomic mass number, e.g.,  $Z = 6$  for carbon. Summarizing,  $Z$  describes the *chemical* classification and  $\rho$  the *physical* morphology of the absorbing material.

The  $\rho Z$  projection algorithm presented here extracts  $\rho$  and  $Z$  from spectral attenuation measurements with continuous x-ray sources. In the upcoming section we describe the analytical solution as well as the exact numerical treatment. The feasibility, properties, and precision of the algorithm are then examined using spectral CT data.

## II. THEORY OF THE $\rho Z$ PROJECTION

X-ray attenuation for energies  $E < 511$  keV is due to (a) photoeffect absorption, (b) Compton scattering, and (c) Rayleigh scattering. The total spectral attenuation coefficient  $\kappa(E, \rho, Z)$  is given by

$$\kappa = \kappa_{\text{photo}} + \kappa_{\text{Compton}} + \kappa_{\text{Rayleigh}}. \quad (2)$$

<sup>a)</sup> Author to whom correspondence should be addressed; electronic mail: bjoern.heismann@siemens.com

TABLE I. Attenuation of body materials.

Organ or material	Relative attenuation $C$ (HU)
Bone, compact	250– $\gg$ 1000
Bone, spongy	50–200
Liver	50–70
Blood	50–60
Pancreas	30–50
Kidney	20–40
Water, ideal	0
Fat	–60––100
Lung	–550––950
Air, ideal	–1000

For the following analytical approximation,  $\kappa_{\text{Rayleigh}}$  will be regarded as a small negligible contribution. The remaining  $\kappa_{\text{photo}}$  and  $\kappa_{\text{Compton}}$  are linear in the density  $\rho$ . Equation (2) factorizes into  $\rho$  and the mass attenuation coefficient ( $\kappa/\rho$ ):

$$\kappa = \left(\frac{\kappa}{\rho}\right)\rho = \left(\frac{\kappa_{\text{photo}}}{\rho}\right)\rho + \left(\frac{\kappa_{\text{Compton}}}{\rho}\right)\rho. \quad (3)$$

The photoeffect attenuation  $\kappa_{\text{photo}}/\rho$  depends on the atomic number  $Z$  of the absorber (=average number of electrons/atom) and the energy  $E$  of the radiation. To work out the basic ideas, the approximation

$$\left(\frac{\kappa_{\text{photo}}}{\rho}\right) = \alpha \frac{Z^k}{E^l} \quad (4)$$

with  $\alpha = \text{const}$  is used here. Classically,  $k=3$  and  $l=3$ ; for numerical fits of experimental data  $k$  lies between 3 and 4, and  $l$  between 3 and 3.5 (see, e.g., Cho *et al.*<sup>4</sup>).

The Compton scattering attenuation  $\kappa_{\text{Compton}}/\rho$  is in good approximation independent of  $Z$  and  $E$  for  $E < 140$  keV:

$$\left(\frac{\kappa_{\text{Compton}}}{\rho}\right) = \beta \approx 0.02 \text{ m}^2/\text{kg}. \quad (5)$$

Substituting Eqs. (4) and (5) into Eq. (2) yields

$$\kappa(E, \rho, Z) = \alpha \rho \frac{Z^k}{E^l} + \beta \rho. \quad (6)$$

It is important to note that  $\kappa$  is a steady monotonic function of  $\rho$  and  $Z$  for nonzero  $E$ . The higher  $E$ , the more  $\kappa$  is ruled by Compton scattering, i.e., the density  $\rho$  of the absorber. At lower energies the photoeffect and thus the atomic number  $Z$  tends to dominate. For notational simplicity, the dependency of  $\kappa$  on  $\rho$  and  $Z$  will not be denoted explicitly in the following.

The energy dependence of Eq. (6) provides the principle of our  $\rho Z$  projection. Consider measuring  $\kappa$  at two different energies  $E_1, E_2$ , thought to be ideally monochromatic. From Eq. (6) one obtains

$$\begin{pmatrix} \kappa_1(E_1) \\ \kappa_2(E_2) \end{pmatrix} = \begin{pmatrix} \beta & \frac{\alpha}{E_1^l} \\ \beta & \frac{\alpha}{E_2^l} \end{pmatrix} \cdot \begin{pmatrix} \rho \\ \rho Z^k \end{pmatrix}. \quad (7)$$

Equation (7) can directly be inverted and solved for  $\rho$  and  $Z$ . This straightforward two-energy approach can be used for  $\gamma$ -source measurements (see, e.g., Rizescu *et al.*<sup>5</sup>).

However, in x-ray measurements one rather works with a continuous tube spectrum  $S(E)$  and detector sensitivity  $D(E)$ ,  $0 < D(E) < 1$ . By defining the effective attenuation coefficient  $\mu$  as

$$\begin{aligned} \mu &= \lim_{d \rightarrow 0} \left[ -\frac{1}{d} \ln \left( \frac{I}{I_0} \right) \right] \\ &= \lim_{d \rightarrow 0} \left[ -\frac{1}{d} \ln \left( \frac{\int S(E) D(E) e^{-\kappa(E)d} dE}{\int S(E) D(E) dE} \right) \right], \end{aligned} \quad (8)$$

we obtain

$$\mu = \int w(E) \kappa(E) dE \quad (9)$$

with the weighting function

$$w(E) = \frac{S(E) D(E)}{\int S(E) D(E) dE}. \quad (10)$$

For measured effective attenuation coefficients  $\mu$  we deal with another level of approximation. We have  $\int_L \mu(\vec{r}) d\vec{r} = \ln \{ \int w(E) \exp[-\int_L \kappa(E, \vec{r}) dl] dE \}$  as the quantity measured by x-ray attenuation methods like CT, with the integrals  $\int_L \dots$  taken along paths  $L$  of the x rays. We again obtain Eq. (9) when approximating  $\exp(\dots)$  for shorter paths i.e. small objects.

It is important to note that the effective  $\mu$  depends on the system parameters  $S(E)$  and  $D(E)$ . This explains the difficulty of using  $\mu$  as an absolute quantitative value mentioned in the Introduction.

With Eq. (9) we obtain the set of integral equations

$$\begin{pmatrix} \mu_1 \\ \mu_2 \end{pmatrix} = \rho \cdot \begin{pmatrix} \int w_1(E) \left(\frac{\kappa}{\rho}\right)(E, Z) dE \\ \int w_2(E) \left(\frac{\kappa}{\rho}\right)(E, Z) dE \end{pmatrix}, \quad (11)$$

which has to be inverted for  $\rho$  and  $Z$ :

$$\begin{pmatrix} \mu_1(\rho, Z) \\ \mu_2(\rho, Z) \end{pmatrix} \rightarrow \begin{pmatrix} \rho(\mu_1, \mu_2) \\ Z(\mu_1, \mu_2) \end{pmatrix}. \quad (12)$$

Equations (11) and (12) express the basic idea of the  $\rho Z$  projection. From an experimental point of view, the two  $\mu_1, \mu_2$  needed for Eq. (11) may originate from different setups: The x-ray tube spectrum  $S(E)$  and the detector sensitivity  $D(E)$  are commutative in Eq. (10). This means we can generate the spectral data by (a) *two* measurements with different x-ray source spectra  $S_i(E)$ ; (b) *two* measurements with different detector sensitivities  $D_i(E)$ ; or (c) *one* measurement with an energy-resolving detector, i.e., different spectral detector sensitivities  $D_i(E)$  are realized at once.

Figure 1 shows the  $S_i(E)$ ,  $D(E)$ , and  $w_i(E)$  of the experimental section as an example for case (a). Two different source spectra and one detector sensitivity yield two different  $w_1(E), w_2(E)$ .

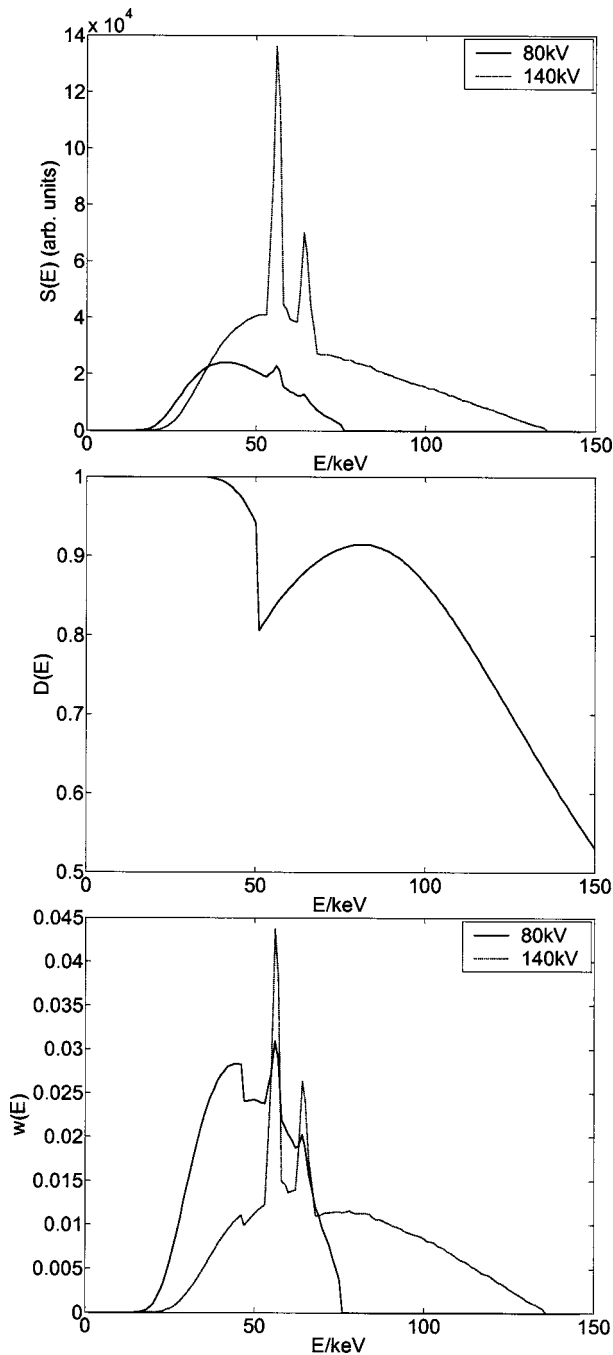


FIG. 1.  $S_1(E)$  and  $S_2(E)$  (top),  $D(E)$  (center), and resulting  $w_1(E)$  and  $w_2(E)$  (bottom) used in the experimental section. The source spectra  $S_{1,2}(E)$  are simulated curves for two tube voltages  $U_1=80$  kV and  $U_2=140$  kV (see the experimental section for the slightly different prefiltering). The detector efficiency  $D(E)$  has been calculated for the 1.4 mm GdOS scintillator used in the CT detector. The  $w_i(E)$  result from Eq. (10).

In the following we provide an approximate analytical and a precise numerical solution to Eqs. (11) and (12) and also define effective  $\rho$  and  $Z$  values for compounds.

### A. Approximate analytical $\rho Z$ projection

Substituting Eq. (6) into Eq. (11) yields

$$\begin{pmatrix} \mu_1 \\ \mu_2 \end{pmatrix} = \begin{pmatrix} \beta & g_1 \\ \beta & g_2 \end{pmatrix} \cdot \begin{pmatrix} \rho \\ \rho Z^k \end{pmatrix} \quad (13)$$

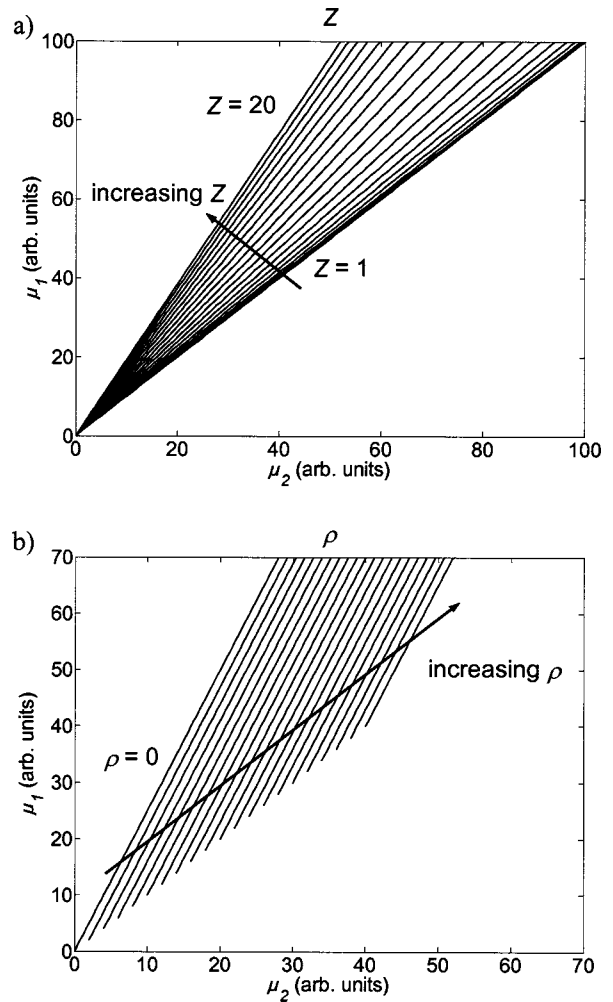


FIG. 2. Contour plots of the analytic  $\rho Z$  projection. (a) shows  $Z = \text{const}$  and (b) shows  $\rho = \text{const}$  as a function of  $\mu_1, \mu_2$  according to Eqs. (16) and (17) with  $g_1 = \alpha \times 10^{-5}$  and  $g_2 = 0.4 \alpha \times 10^{-5}$ .  $\mu_1 > \mu_2$  follows from  $g_1 > g_2$  [see Eq. (13)]. The  $g_i$  are calculated from Eq. (14) with the  $w_i(E)$  taken from the experimental section (Fig. 1).

with

$$g_i = \alpha \int \frac{w_i(E)}{E^l} dE. \quad (14)$$

Equation (13) is inverted to

$$\begin{pmatrix} \rho \\ \rho Z^k \end{pmatrix} = \frac{1}{\beta(g_2 - g_1)} \begin{pmatrix} g_2 & -g_1 \\ -\beta & \beta \end{pmatrix} \begin{pmatrix} \mu_1 \\ \mu_2 \end{pmatrix}. \quad (15)$$

This yields

$$\rho = \frac{1}{\beta} \frac{g_2 \mu_1 - g_1 \mu_2}{g_2 - g_1} \quad (16)$$

and

$$Z = \left( \beta \frac{\mu_2 - \mu_1}{g_2 \mu_1 - g_1 \mu_2} \right)^{1/k} = \left( \beta \frac{1 - \mu_1/\mu_2}{g_2 \mu_1/\mu_2 - g_1} \right)^{1/k}. \quad (17)$$

$\rho$  is a weighted difference of  $\mu_1, \mu_2$  whereas  $Z$  is a non-linear function of the ratio  $\mu_1/\mu_2$ . Figures 2(a) and 2(b)

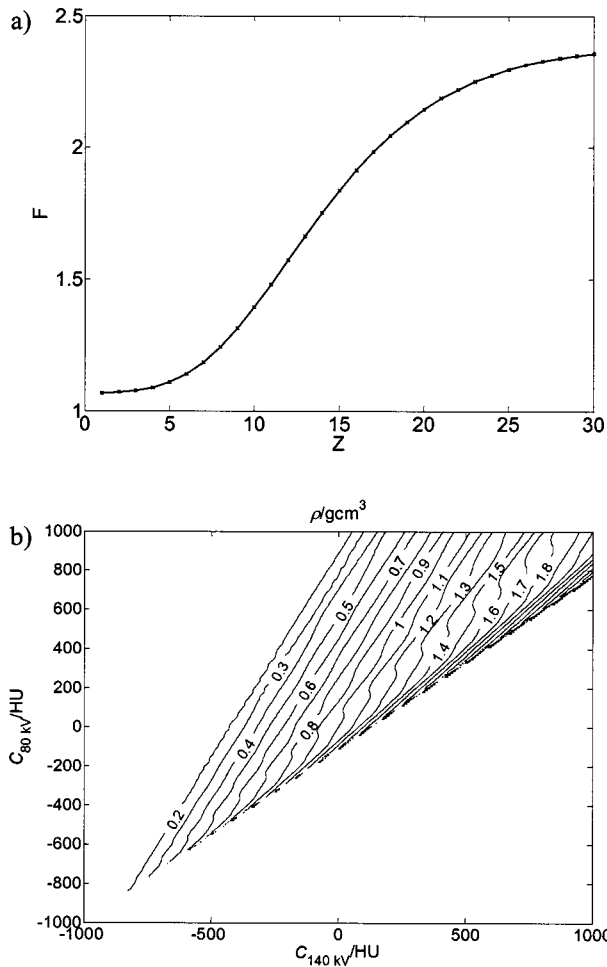


FIG. 3. Plots of the numerical results of the  $\rho Z$  projection. (a) shows  $F(Z)$  of Eq. (18) and (b) displays  $\rho(C_{80\text{ kV}}, C_{140\text{ kV}})$  of Eq. (20). We have used the  $w_i(E)$  of Fig. 1 and the water normalization of Eq. (1).

show contour plots of Eqs. (16) and (17) with  $k=3$ . The  $Z = \text{const}$  and  $\rho = \text{const}$  lines reflect the difference in the functional dependencies.

**B. Numerical  $\rho Z$  projection**

The analytical results of the  $\rho Z$  projection in Eqs. (16) and (17) are limited by the precision of the approximation (6). In order to obtain exact results, we use numerical tables for the spectral mass attenuation coefficients  $(\kappa/\rho)(E, Z)$  (see, e.g., Perkins *et al.*<sup>6</sup> and Cullen *et al.*<sup>7</sup>). Then Eq. (11) yields the atomic number  $Z$  as

$$\frac{\mu_1}{\mu_2} = \frac{f_1(Z)}{f_2(Z)} = F(Z) \Rightarrow Z = F^{-1}\left(\frac{\mu_1}{\mu_2}\right) \tag{18}$$

with

$$f_i(Z) = \int w_i(E) \left(\frac{\kappa}{\rho}\right)(E, Z) dE \tag{19}$$

and the density

$$\rho = \frac{\mu_1}{f_1(Z)} = \frac{\mu_1}{f_1[F^{-1}(\mu_1/\mu_2)]}. \tag{20}$$

Equations (18)–(20) represent the numerical  $\rho Z$  projection. For  $Z$  in Eq. (18), Fig. 3(a) shows  $F(Z)$  for integer  $Z = 1, 2, \dots, 30$  with the  $w_i(E)$  of Fig. 1. Since  $F(Z)$  is a monotonically rising function of  $Z$  for this interval, we can calculate the inverse function  $Z = F^{-1}(\mu_1/\mu_2)$  by numerical interpolation. As in the analytical approximation (17), this numerical definition of a fractional  $Z$  is a one-dimensional function of the measured attenuation ratio  $\mu_1/\mu_2$ .

The density  $\rho$  in Eq. (20) is still a two-dimensional function of  $\mu_1$  and  $\mu_2$ . Figure 3(b) depicts a contour plot of  $\rho(\mu_1, \mu_2)$  with the  $w_i(E)$  of Fig. 1.  $\mu_1$  and  $\mu_2$  have been normalized to CT values  $C_{80\text{ kV}}$  and  $C_{140\text{ kV}}$  according to Eq. (1); see also the next section.

The numerical results for  $\rho$  in Fig. 3(b) are in good agreement with the analytic results of Fig. 2(b). Major differences occur for larger  $\rho$ . This mainly demonstrates the limits of the analytic approximation of energy-independent Compton scattering.

**C. Definition of  $\rho$  and  $Z$  for heterogeneous materials**

For a mixture of chemical elements with densities  $\rho_i$ , the overall effective  $\rho_{\text{eff}}$  is defined by

$$\rho_{\text{eff}} = \sum_i \rho_i, \tag{21}$$

where  $\rho_i$  is just the partial chemical density created by the atoms of element  $i$  alone. This relies on the fact that for  $x$  rays in the medical diagnostic energy range  $E < 140$  keV, adding photon cross sections of individual elements approximates the interaction between photons and composite matter very well.<sup>8</sup>

The definition of an effective  $Z$  follows from this. With the analytical approximation of the attenuation coefficient (6) one obtains

$$\kappa(E, \rho_{\text{eff}}, Z_{\text{eff}}) = \alpha \rho_{\text{eff}} \frac{Z_{\text{eff}}^k}{E^l} + \beta \rho_{\text{eff}} \tag{22}$$

with

$$Z_{\text{eff}}^k = \frac{\sum_i Z_i^k \rho_i}{\sum_i \rho_i}. \tag{23}$$

For water,  $Z_H=1$ ,  $Z_O=8$ ,  $\rho_O=8\rho_H$ , and Eq. (23) yields  $Z_{\text{eff}, H_2O} \approx 7.45$  for  $k=3$ . In the upcoming sections we will use  $Z$  in the sense of an effective  $Z$  definition.

A sum rule for the spectra is obtained by inserting Eq. (21) into

$$\mu(\rho_{\text{eff}}, Z_{\text{eff}}) = \int w(E) \rho_{\text{eff}} \left(\frac{\kappa(E)}{\rho}\right)_{\text{eff}} dE. \tag{24}$$

This yields

$$\left(\frac{\kappa(E)}{\rho}\right)_{\text{eff}} = \frac{\sum_i \rho_i [\kappa(E)/\rho]_i}{\rho_{\text{eff}}}. \tag{25}$$

The hydrogen and oxygen spectra have been summed accordingly to calculate the water normalization (1) in Fig. 3.

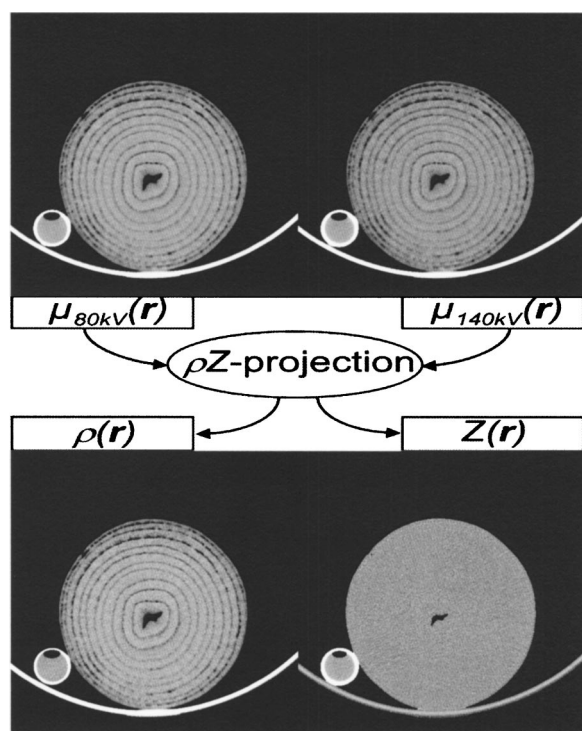


FIG. 4. Original 80 kV, 140 kV, and  $\rho Z$ -projected CT images of an onion. A glass cylinder with water has been added for calibration. The 80 kV and 140 kV images use a gray-scale window from black to white of  $[-200 \text{ HU}, 200 \text{ HU}]$ . Lower values are clipped as black, higher values are clipped as white. The  $\rho$  image uses  $[0.75 \text{ g/cm}^3, 1.25 \text{ g/cm}^3]$  and the  $Z$  image  $[4, 11]$ . Note the “soft” character of the  $\rho$  image compared to the  $Z$  image. This is due to partial volume material that images smoothly in the  $\rho$  image (see also Fig. 5) whereas it produces sharp material/air borders in the  $Z$  image. The thinner representation of the glass housing in the  $\rho$  image is based on this: the outer partial volume pixels are shown as black in this gray-scale window.

### III. EXPERIMENT

We obtained spectral data with two measurements using different source spectra  $S_i(E)$  on a commercial multislice CT scanner (Siemens Sensation 4 CT, Siemens Forchheim, Germany). The tube voltages and prefiltering of the x-ray spectrum were (1)  $U_1 = 80 \text{ kV}$  tube voltage with 0.6 mm titanium prefiltering and (2)  $U_2 = 140 \text{ kV}$  with 1.2 mm Ti pre-filtering. The different Ti filter settings further shift the 140 kV spectrum to higher energies compared to the 80 kV spectrum. See Fig. 1 for a plot of the resulting  $S_i(E)$ .

In the following we present the results of two measurements. Both were performed in static slice mode of the CT and transformed into  $\rho$  and  $Z$  images with the numerical  $\rho Z$  projection algorithm.

(a) An organic sample (onion) demonstrates the basic feasibility and properties of the method (Figs. 4 and 5).

(b) A set of water solutions of chemicals with known densities and compositions yields data on the absolute precision (Table II, Figs. 6 and 7).

### IV. RESULTS

We start with the images in Fig. 4 of an onion. The two original CT pictures (top) and the transformed  $\rho(\mathbf{r})$  and  $Z(\mathbf{r})$  (bottom) are shown.  $\rho(\mathbf{r})$  looks similar to the original HU picture. But instead of relative and qualitative HU values and

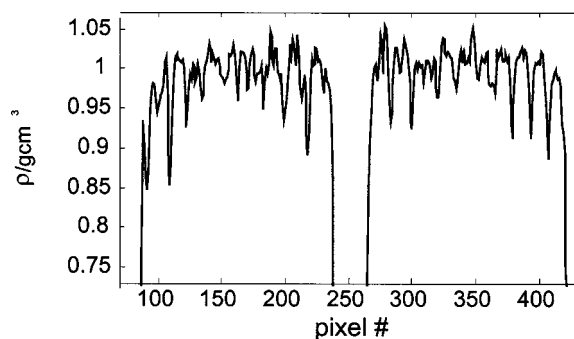


FIG. 5. Radial density distribution of the onion of Fig. 4, taken at a horizontal line through its center. The periodic shell structure is readily observed.

gradients, one obtains quantitative values for  $\rho$ . As an example, the radial density of the onion is shown in Fig. 5. The periodic structure of the onion shells is measured with absolute density values.

Interestingly, the shells are not represented in the  $Z(\mathbf{r})$  image. Only the hole corresponding to the small air cavity at the center of the onion can be found. In order to understand this, consider a volume of a homogeneous solid material like, e.g., carbon. When the number of atoms/volume decreases due to adding pores or changing atomic structure,  $\rho = dm/dV$  decreases too. But  $Z = \text{number of electrons/atom}$  of the solid stays constant. Air filling the pores under atmospheric conditions has no significant impact on the overall effective  $Z$  since the difference between molecules per volume of a gas and a solid is around  $\sim 10^5$ .

If no solid is present,  $Z$  cannot be calculated from tiny gas attenuations (see the convergence of the  $Z = \text{const}$  lines for small attenuations in Fig. 3). The  $Z = 0$  hole at the center of the onion represents a nonavailable number.

So it is important to note that one measures the  $Z$  of the solid. For the onion, this yields a homogeneous value  $Z(\text{onion}) = 7.20$  for the onion cell material. This is  $\sim 0.25$  below the level of  $Z(\text{water}) = 7.45$ .

A gradient in  $Z$  can also be observed. The head holder of the CT system is represented as the curved line below the onion. It has a  $Z$  of 7.1 on the surface rising to 8.1 in the center. This reflects its glass-fiber material composition. An organic matrix is filled with an increasing density of glass-fiber bundles toward the center. The effective  $Z$  changes accordingly.

To investigate the absolute precision of the  $\rho$  and  $Z$  values, we measured samples with known  $\rho$  and  $Z$ . Water solutions of various chemicals were used. Table II lists the chemicals and their mass ratios to water. It includes the  $\rho$  taken from the chemical preparation and the  $Z_{\text{eff}}$  calculated according to the approximate formula (23) with  $k = 3$  (classical approximation).

We used cross-sectional CT images of glass cylinders filled with the solutions to calculate the  $\rho Z$ -projected images in Fig. 6.  $\rho$  and  $Z$  were averaged over 150 central pixels of the cross-sectional circle surface. The results are listed in Table II for comparison with the chemical preparation values. The deviations  $\Delta\rho$  and  $\Delta Z$  between CT measurements and chemical data are plotted in Fig. 7.

TABLE II. Density and effective  $Z$  of various chemicals dissolved in water as measured and calculated from chemical preparation and  $\rho Z$  measurement. Deviations are shown graphically in Fig. 6.

#	Chemical dissolved in water	Chemical concentration (wt %)	Chemical density ( $\text{g cm}^{-3}$ )	CT measured density ( $\text{g cm}^{-3}$ )	$ \Delta\rho $ ( $\text{g cm}^{-3}$ )	Approx. chemical $Z_{\text{eff}}$	CT measured $Z_{\text{eff}}$	$ \Delta Z_{\text{eff}} $
1	NH <sub>3</sub>	5	0.978	0.980	0.002	7.37	7.46	0.09
2		10	0.958	0.960	0.002	7.32	7.42	0.10
3		25	0.910	0.916	0.006	7.21	7.23	0.02
4	HNO <sub>3</sub>	16	1.092	1.078	0.014	7.47	7.51	0.04
5		31	1.187	1.156	0.031	7.49	7.53	0.04
6	NaOH	10	1.111	1.093	0.018	7.68	7.72	0.04
7		20	1.219	1.189	0.030	7.89	7.94	0.05
8	KOH	15.7	1.145	1.132	0.013	9.84	9.41	0.43
9	LiOH	6.7	1.062	1.061	0.001	7.41	7.46	0.05
10	H <sub>2</sub> O <sub>2</sub>	30	1.10	1.090	0.010	7.49	7.58	0.09
11	FeSO <sub>4</sub> ·7H <sub>2</sub> O	5.6	1.031	1.050	0.019	8.39	8.47	0.08
12	H <sub>2</sub> SO <sub>4</sub>	29	1.209	1.240	0.031	8.74	8.95	0.21

For  $\rho$ , the statistical deviations are in the range of  $\sigma_{\rho} = 20 \text{ mg/cm}^3$ . The finer structures in Fig. 5 thus represent actual sample properties and are not attributed to noise.

$Z$  shows a major deviation for the KOH measurement. This could be due to (a) the limited precision of the  $k=3$  value in Eq. (23) for higher  $Z$  or (b) CO<sub>2</sub> absorption in the KOH used for preparation, which could lower the solution's chemical  $Z$  toward the CT-measured value. Statistically, the chemical  $Z$  values are reproduced with a precision in the range of  $\sigma_Z = 0.1$ .

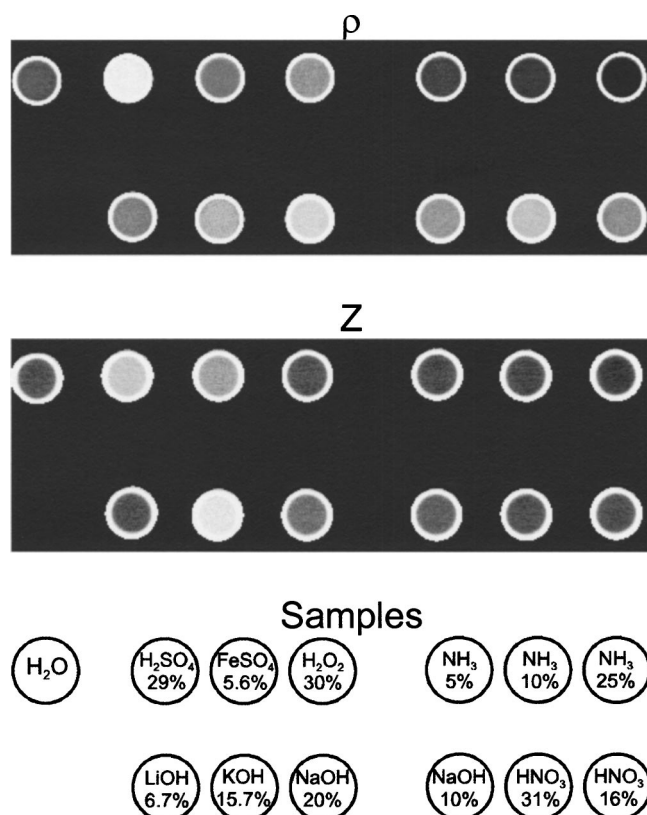


FIG. 6. Chemical sample measurement used for estimating the precision of  $\rho Z$ -transformed CT data. Quantitative values extracted from these images are listed in Table II.

## V. SUMMARY

We developed the  $\rho Z$  projection as an x-ray method for measuring the density  $\rho$  and the atomic number  $Z$  of a scanned object. Its main feature is to express both  $\rho$  and  $Z$  as a direct function of at least two attenuation values  $\mu_1, \mu_2$  with different spectral weighting. The weighting differences

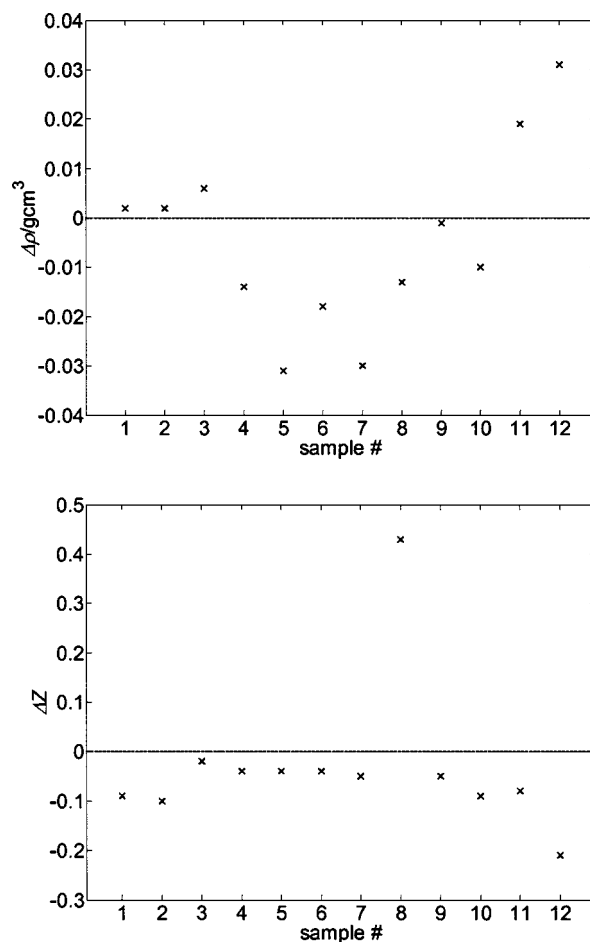


FIG. 7. Deviations of density and atomic number values between CT measurement and chemical preparation values.

can be realized by the x-ray source as well as by detector sensitivity modifications. The latter also covers energy-resolving detectors.

We obtained quantitative and absolute values in comparison to the relative use of attenuation measurements. The experimental CT data for an organic sample, for example, quantifies the density variations in an onion shell structure and the effective  $Z$  transition in a glass-fiber sample holder.

Furthermore, the images illustrate the complementary meaning of  $\rho$  and  $Z$ . The  $\rho$  image has a smooth character, reflecting the continuous density variations in the cell structures, whereas  $Z$  shows sharp material transitions. This stresses that the density  $\rho$  is given *per volume* and  $Z$  is given *per atom or molecule*. We achieve a fundamental separation into  $Z$  as a chemical and  $\rho$  as a morphological quantity.

The precision of the method for CT has been evaluated with water solutions of several chemical substances with effective  $Z$  between 7.2 and 9.8 and  $\rho$  between 0.91 and 1.24

$\text{g/cm}^3$ . For this range we found absolute precisions of  $\Delta\rho = 20 \text{ mg/cm}^3$  and  $\Delta Z = 0.1$ . We estimate that it can be further increased by improved spectral measurement techniques.

Considering these results, we conclude that the  $\rho Z$  projection provides a further class of precise information for quantitative x-ray applications.

<sup>1</sup>A. S. Agatston, W. R. Janowitz, F. J. Hildner, N. R. Zusmer, M. Viamonte, and R. Detrano, *J. Am. Coll. Cardiol.* **15**, 827 (1990).

<sup>2</sup>H. K. Genant and D. Boyd, *Invest. Radiol.* **12**, 545 (1977).

<sup>3</sup>R. E. Alvarez and A. Macovski, *Phys. Med. Biol.* **21**, 733 (1976).

<sup>4</sup>Z. H. Cho, Z. M. Tsai, and G. Wilson, *Phys. Med. Biol.* **11**, 225 (1975).

<sup>5</sup>C. Rizescu, C. Besliu, and A. Jipa, *Nucl. Instrum. Methods Phys. Res. A* **465**, 584 (2001).

<sup>6</sup>S. T. Perkins, D. E. Cullen, M. H. Chen, J. H. Hubbell, J. A. Rathkopf, and J. H. Scofield, Report No. UCRL-50400, Vol. 30, 1991.

<sup>7</sup>D. E. Cullen, M. H. Chen, J. H. Hubbell, S. T. Perkins, E. F. Plechaty, J. A. Rathkopf, and J. H. Scofield, Report No. UCRL-50400, Vol. 6, Rev. 4, 1989.

<sup>8</sup>H. H. Barrett and W. Swindell, *Radiological Imaging*, Vol. 1 (Academic, New York, 1981).